Axial-Flux Permanent-Magnet Synchronous Generator with Coreless Armature and Non-Integral Coil-Pole Ratio

Danqi Wu[1], Junhua Yang[1], Tze Fun Chan[2], Chun Sing Lai[1,3] ✉, Xuecong Li[1] ✉, Baiping Yan[1], Loi Lei Lai[1], Dongxiao Wang[1], Xiaodan Gao[4], Ke Meng[5]

1School of Automation, Guangdong University of Technology, Guangzhou, Guangdong 510006, People's Republic of China
2Department of Electrical Engineering, Hong Kong Polytechnic University, Hong Kong, SAR China
3School of Civil Engineering, University of Leeds, UK
4Lloyd's Register Australia, Melbourne, VIC 3000, Australia
5School of Electrical Engineering and Telecommunications, University of New South Wales, Sydney, NSW 2052, Australia
✉ *Corresponding authors emails: wudanqi1022@163.com (X. Li), c.s.lai@leeds.ac.uk (C. S. Lai)*

Abstract: This paper presents a study on an Axial-Flux Permanent-Magnet Synchronous Generator (AFPMSG) with a double-sided rotor, coreless armature. The armature winding consists of nonoverlapping concentrated coils and has a non-integral coil-pole ratio. It is shown that, with an appropriate choice of armature coil number to pole number, the fundamental winding factor of the AFPMSG can be made close to that of a full-pitched integral slot winding. The field distribution and load performance are computed for a prototype machine based on a two-dimensional, time-stepping finite element method. A study of the armature reaction effect of the coreless armature winding and the origin of torque ripple is also carried out. The computed voltage and current waveforms, as well as the load characteristics, are verified by practical experiments.

Index Terms: Axial-flux, permanent-magnet generator, finite element analysis.

1 Introduction

With the increasing demand for energy, non-renewable energy resources are depleting rapidly, and their consumption is also causing changes to the earth's climate. To prevent major energy crisis and reduce CO_2 emissions, it is extensively considered that wind power generation is one of the most promising solutions to the energy crisis and climate change [1-3]. Global Wind Energy Council has reported that the global installed wind power reached 496.9 GW in 2016 [4]. The big markets of China, the US and Canada get 4%, 5.5%, and 6% of their power from wind, respectively [5]. It is expected that the wind power will supply up to 20% of the global electricity generation by 2030 [6]. In Denmark, wind power produced the equivalent of 43.4% of its total electricity consumption in 2017. It is estimated to increase the share of electricity production from wind to 50% by 2020, and to 84% by 2035 [7].

AFPMSG has been used and studied a lot for direct-coupled wind turbine energy conversion system [8-17]. Besides, its use as a high-frequency generator and automotive application has also been proposed [18-21]. An axial-flux machine has the advantages of winding design, better cooling, the possibility of modular construction and more flexible field as compared to a radial-flux one [8]. Among the various machine designs, the double-sided configuration, in which a disk stator winding is sandwiched between two permanent-magnet rotors, is the most popular because of its high-power density. Coreless armature designs [10,11,12] have been adopted to reduce the armature iron loss as well as the magnetic pull between the field and the armature. A larger volume of high-energy permanent-magnet materials [17] is required for the field system, due to the large effective air gap. Though AFPMSGs with coreless armature has better efficiencies when operated at high frequencies [18,19], these machines are also widely used for small-scale, low-speed, direct-drive wind energy conversion systems because of their compactness, straightforward construction, and reduced weight [11,14].

Cogging torque can also be eliminated by using the 'torus' design as detailed in [9], [11] and [16]. The armature winding is wound on a laminated toroidal iron core, giving a toothless structure. High power density is possible due to presence of armature iron core, but construction of the armature winding presents considerable difficulties as pre-formed coils cannot be used [22]. Magnetic pull between the stator and rotor can be severe unless the effective air gaps are equal on both sides of the armature.

Axial-flux permanent-magnet machines provide more flexibility in the choice of rotor pole and armature coil shapes [22,23,24]. Trapezoidal magnets are used in many axial-flux machines [25], but circular (cylindrical) magnets have also been adopted in generators for wind energy [12] and automotive [21] applications. In a like manner, armature coils of axial-flux machines can be trapezoidal [10], circular [21], and rhomboidal [18].

Kamper *et al.* [26] has studied axial-flux permanent-magnet machines with air-cored non-overlapping concentrated stator windings. It is shown that a concentrated-coil winding machine can have a similar performance as that of a normal overlapping winding machine. The work also studies the effect of coil number to pole number on the winding factor and output torque. It is found that a winding and with one coil in a phase band and in which the number of poles is divisible by four has the highest winding factor. Compared with a normal overlapping winding, the end-turn length of a non-overlapping winding is shorter, hence less copper is required for a given power output. The armature resistance is smaller, resulting in reduced armature copper loss and voltage regulation.

In this paper, a detailed study on an AFPMSG with double-sided rotor, coreless armature, and non-overlapping concentrated-coil winding with non-integral coil-pole ratio will be conducted. The prototype machine is conceived as a small direct-driven wind turbine generator. To produce a frequency of 50 Hz at a speed of 375 r/min, the generator must be constructed with 16 poles. The optimal coil-pole ratio, according to [26], should be 3:4, hence the armature winding should consist of 12 coils.

Certain methods have been adopted to analyse the magnetic field and performance of axial-flux permanent-magnet machines. These include quasi-three-dimensional analytical methods [11,14,27,28], three-dimensional finite element analysis (3-D FEA) [15,16,28,29], two-dimensional analytical methods [25,30], and two-dimensional finite element analysis (2-D FEA) [30]. Analytical methods are efficient and the effect of machine parameters on the resultant field can be easily studied, but their use is generally limited to the study of

no-load flux density distribution in machines with simple geometries. For the study of generator performance on load, FEA is to be preferred. Field solution of the AFPMSG is strictly speaking a 3-D problem, but 3-D FEA is computationally very demanding and the solution time is extremely long when the number of elements is large and a time-stepping coupled circuit analysis is involved. This is the case with the prototype AFPMSG in which the magneto-motive force (m.m.f) distribution is asymmetrical with respect to each rotor pole. For periodic conditions to be applied, the geometric model has to cover a region of four pole-pitches. A 2-D FEA will therefore be used for magnetic field study on the prototype AFPMSG. A time-stepping, coupled field-circuit approach is used for analysing the armature reaction, torque, and performance of the machine on load.

The remainder of this paper is organized as follows. Section 2 describes the main design features of the prototype AFPMSG and the computation of winding factor. Section 3 formulates the modeling approach for time-stepping coupled field-circuit FEA. In Section 4, the computed results, including field components on no load, armature reaction field, torque, and generator waveforms on load are given. Section 5 incorporates the experimental results and presents a comparison with simulation results. Section 6 concludes the paper.

2 Prototype AFPMSG

A prototype Axial-Flux Permanent-Magnet Synchronous Generator (AFPMSG) with double-sided rotor shown in Fig. 1 was designed and constructed for the present study. The machine dimensions were determined using the approach outlined in [14], the ratio of outer to inner diameter being close to $\sqrt{3}$ for optimum power output. As shown in Fig. 2, each rotor disk carries 16 trapezoidal-shaped NdFeB magnets, while the stator disk consists of 12 single-layer, non-overlapping coils. The end windings are approximately circular arcs. Adjacent coil sides are placed side by side to give a better utilization of space. In an adopted coreless winding design, the coils are encapsulated in epoxy-resin to give the required mechanical strength. The armature disk is fastened to the stationary mechanical supports by using threaded rods which also facilitate fine adjustment of the mechanical clearance on each side of the armature winding during assembly of the machine (Fig. 1).

For the evaluation of the winding factor, an AFPMSG with p pole-pairs and N armature coils is considered. Each coil side has a circumferential width w. From Fig. 2, it is apparent that the armature winding has a fundamental distribution factor K_{d1} equal to unity, as coils of the same phase occupy the same relative position under each rotor magnetic pole. Each coil side, however, is distributed due to the spread of the conductors along the circumferential direction. The fundamental coil side spread factor K_{cs1} is defined by

$$K_{cs1} = \frac{\tau_p \sin\left(\frac{w}{\tau_p}\pi\right)}{w\pi} \tag{1}$$

where τ_p is the pole pitch at the mean diameter D, given by

$$\tau_p = \frac{\pi D}{2p} \tag{2}$$

From Fig. 2, the coil span β_c, computed at the mean diameter D, is given by

$$\beta_c = \left(\frac{\pi D/N - w}{\tau_p}\right)\pi \tag{3}$$

The fundamental coil span factor K_{p1} of the AFPMSG is thus

$$K_{p1} = \sin\frac{\beta_c}{2} = \sin\left(\frac{\pi D/N - w}{\tau_p}\right)\frac{\pi}{2} \tag{4}$$

The fundamental winding factor K_{w1} is

$$K_{w1} = K_{p1}K_{d1}K_{cs1} \tag{5}$$

For the prototype generator, N = 12, $2p$ = 16, D = 158 mm, w = 10 mm, hence K_{p1} and K_{cs1} are equal to 0.9998 and 0.9957, respectively. The fundamental winding factor is thus close to unity, which implies that the winding is equivalent to a full-pitched, concentrated winding as far as the fundamental e.m.f. is concerned.

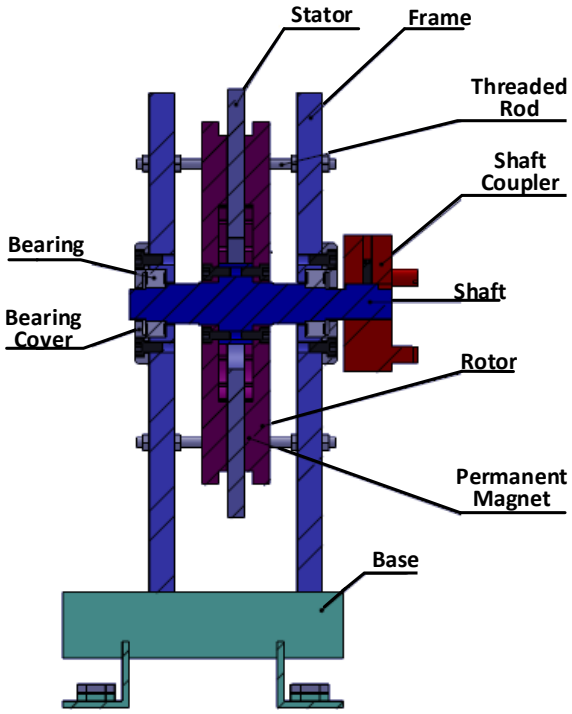

Fig. 1 *Prototype AFPMSG with double-sided rotor and coreless armature*

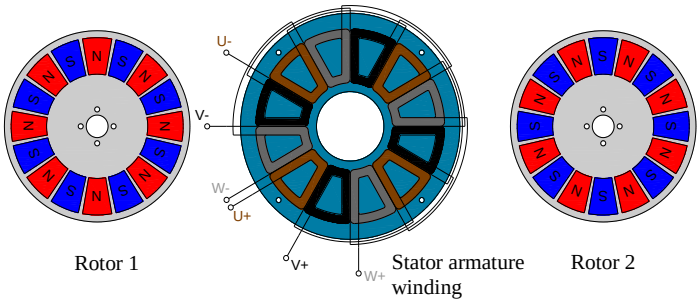

Fig. 2 *Principal components of prototype AFPMSG*

3 Finite Element Analysis

The two-dimensional (2-D) finite element transient solver of ANSYS Version 11 SP1 was adopted as the analysis tool. To compute the generator performance on load, a time-stepping analysis [31] is conducted.

Maxwell's equations, applied to PMSG domains, will give rise to the following diffusion equations:

$$\begin{aligned} &\nabla\times(\nu\nabla\times A) = 0, && \text{in iron and air gap}\\ &\nabla\times(\nu\nabla\times A) = \tfrac{i_s}{s}, && \text{in armature windings}\\ &\nabla\times(\nu_{PM}\nabla\times A) = \nabla\times(\nu_{PM}B_r), && \text{in permanent magnets} \end{aligned} \tag{6}$$

where A, ν, i_s, S, B_r and ν_{PM} are magnetic vector potential, reluctivity, armature phase current, total cross-sectional area of one turn, remanent flux density of the PM and equivalent reluctivity,

respectively.

From Fig. 2, it is apparent that the AFPMSG has a non-integral ratio of coil number to pole number. The armature winding is similar to a fractional slot winding with characteristic ratio 1/*y*, where $y = 4$. That is, the winding repeats itself over a distance of four pole-pitches. This suggests that for periodic conditions to be applied, the time-stepping FE model has to include at least four poles. In order to reduce the scale of the problem, two-dimensional finite element analysis (2-D FEA) will be conducted for a cutting plane at the mean diameter of the generator. Fig. 3 shows the geometric model and the FE mesh for the analysis, where A is the outer surface of the upper rotor and B is a plane mid-way through the armature disk winding. It should be noted that only one-eighth of the machine is modeled, but as the solution region is large, the iron, permanent magnet and conductor regions are meshed with quadrilateral elements, while the air region is meshed with triangular elements. Fig. 4 shows the detailed meshing for different regions in the geometric model. The air gap is divided into two regions by the sliding surface. The outer air gap region belongs to the outer rotor, while the lower air gap region belongs to the stator. On the sliding surface, the lower surface of the outer rotor and the upper surface of the stator overlap and the two surfaces are meshed with the same number of divisions so that the nodes of the rotor surface and the upper stator surface coincide. There are 360 nodes on the sliding surface, which corresponds to a time-step of 0.111 ms.

There are six armature conductor regions in the FE model in Fig. 3. The nodes of each region comprise three degrees of freedom (DOFs), namely the vector potential A_z, the current (CURR) and the electromotive force (EMF). The EMF and CURR DOF of all the nodes in a given region should each be unified as a single variable in the coupled field-circuit FE computations. The region occupied by the armature phase windings and the field quantities to the external circuit are coupled together. The stranded phase winding is modeled as current source elements each having three nodes. Out of the three nodes, two of them carry voltage DOFs, while the third one carries DOFs for current and EMF.

There are 6617 elements and 16159 nodes in the geometric model. Since there is no flux linkage beyond the rotor yoke, the Dirichlet (tangential) boundary condition is assigned to the upper exterior nodes (surface A). On the other hand, the flux lines cross the mid-plane of the armature winding normally, hence the Neumann boundary condition has to be applied to the lower nodes (surface B). Periodic boundary condition is applied to nodes on the leftmost and rightmost exterior nodes (surfaces C and D). The number of nodes located on Dirichlet boundary is 257, the number of nodes located on the periodic boundary planes is 98, and the number of conductor regions is 6. The total variables are thus 16159-257-98/2+2×6=15865. With the chosen time-step of 0.111 ms, the computing time is about 24.7 h for a typical load on a Sun Microsystems station.

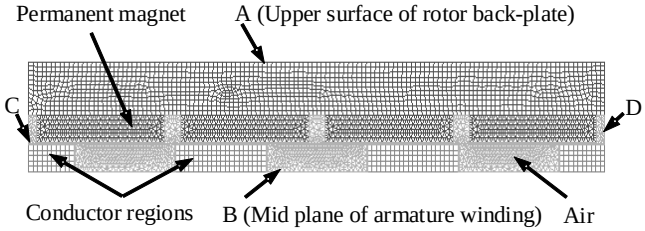

Fig. 3 *Geometric model and meshing of AFPMSG for 2-D FEA. covering the upper half-section of the machine and spanning over four pole-pitches*

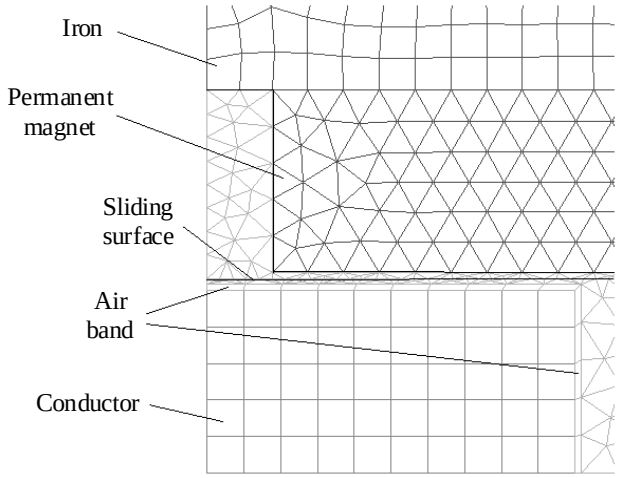

Fig. 4 *Enlarged mesh showing distribution of quadrilateral and triangular elements*

4 Results

A two-dimensional (2-D) finite element analysis (FEA) was conducted for the generator. In the following discussion, θ and z denote the circumferential and axial positions, respectively. The technical data of the prototype generator are shown in the appendix at the end of the paper.

4.1 No-load air gap flux density

The generator has a large effective air gap, thus the armature reaction effect is not strong and the air gap field is approximately equal to that because of the permanent magnets. Computations were conducted utilizing 2-D FEA with the generator on no load. Fig. 5 shows the flux plot of the AFPMSG with double-sided rotor under no-load condition. It is observed that the flux density distribution is symmetrical about the center plane of the stator armature, across which the flux lines pass normally. Null points of flux density also occur on this plane at the interpolar circumferential positions. The flux densities in the rotor back plates are high at interpolar positions. In the subsequent discussion, z denotes field quantities in the axial position, and θ denotes field quantities in the circumferential direction. $z = 0$ corresponds to the mean position of the disk armature winding, while $\theta = 0$ corresponds to an interpolar axis.

Fig. 6 shows the variation of B_z along the circumferential direction at the mean diameter ($D = 158$ mm). In the mean air gap ($z = 5.25$ mm), the waveform is flat-topped, while at the mean position of the disk winding ($z = 0$), the waveform becomes more sinusoidal. Since most of the conductors are within the region -3 mm $< z < 3$ mm, it is expected that the generated e.m.f. of the AFPMSG with double-sided rotor is quite sinusoidal. The waveform of B_z at $z = 8$ mm (magnet region) and $z = 11.5$ mm (rotor back plate) are double-peaked and saddle-shaped, due to the concentration of flux lines at both edges of the magnets.

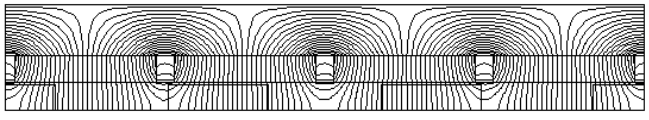

Fig. 5 *Field plot of AFPMSG at no load*

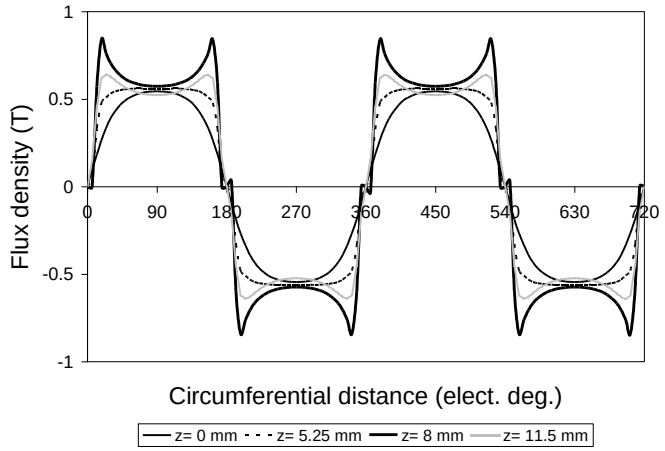

Fig. 6 *Circumferential variation of Bz at the mean diameter (D = 158 mm) when the AFPMSG is on no load*

From Fig. 7, it is observed that B_θ is zero when z = 0. As z increases, B_θ in the interpolar regions increases progressively. In the rotor back plate (z = 11.5 mm), B_θ can reach very high values (~1.4 T). The results indicate that the circumferential component of flux density in the air space is small in an AFPMSG with double-sided rotor, and, except at very high speeds, the eddy current loss in armature conductors should be negligibly small.

The e.m.f. waveform, as well as the harmonic voltages, depends upon the waveform of B_z. Fig. 8 shows the variation of harmonic flux densities with axial position z. It is seen that the third-harmonic component is predominant, followed by the fifth harmonic. In all cases the harmonics increase with axial position z.

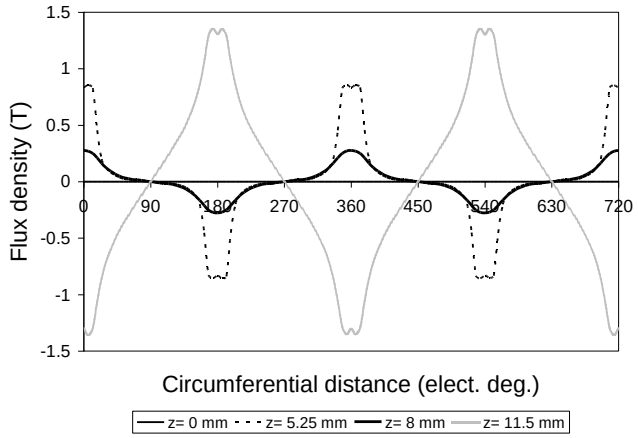

Fig. 7 *Circumferential variation of Bθ at the mean diameter (D = 158 mm) when the AFPMSG is on no load*

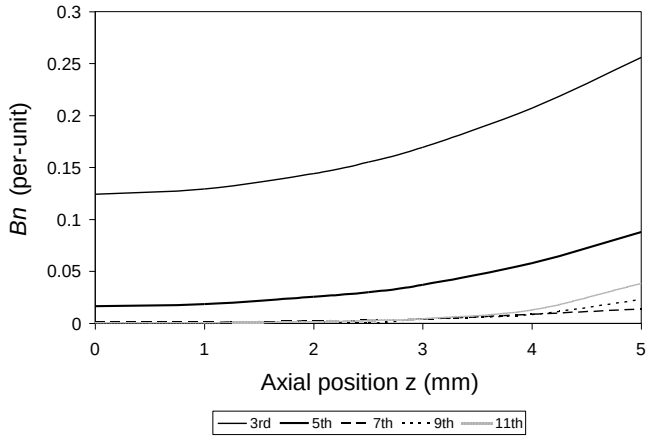

Fig. 8 *Variation of harmonic flux densities with axial position*

4.2 Armature reaction and synchronous reactance

The time-stepping coupled field-circuit method was next used to study the field distribution and electrical performance of the AFPMSG. It is assumed that the speed is constant at the rated value (375 r/min) and balanced rated current is being delivered to a resistive load. Fig. 9 shows the armature reaction flux density in the AFPMSG at the time instant when the instantaneous current in phase A is maximum. The armature reaction flux density is relatively small due to the air-cored winding configuration. Due to the non-integral ratio of coil number to pole number, the flux density distribution is not symmetrical over a physical pole pitch (0~180 degrees). Fig. 10 shows the results of a Fourier analysis conducted flux density distribution in Fig. 8. Because the waveform repeats for every 4 pole pitches (y = 4, an even number), the flux density is an even function and hence even multiples of the lowest-order harmonic component will need to be considered. The integration has to be performed over a cycle of $y\pi$ rad. As shown in Fig. 10, the harmonics are 2/y, 4/y, 8/y, 10/y, 14/y, 16/y, … and so forth. It should also be noted that the component 4/y has a pole pitch that is the same as the rotor pole pitch and hence is the fundamental component in the usual sense, and this component has been used to give the normalized harmonic flux densities in the armature reaction waveform. It is noticed that the most prominent harmonic is the 2/y component, which is 1.34 times the fundamental and which travels at twice of the synchronous speed in the backward direction. With respect to the rotor, this component is thus moving at 3 times the synchronous speed. But since the armature reaction flux density is small (0.021 T for this component), the additional eddy current loss in the back plates and rotor magnet is negligible at rated frequency.

Fig. 11 demonstrates the axial component of the resultant flux density operated under the same condition. A slight asymmetry in the positive and negative half cycles is observed.

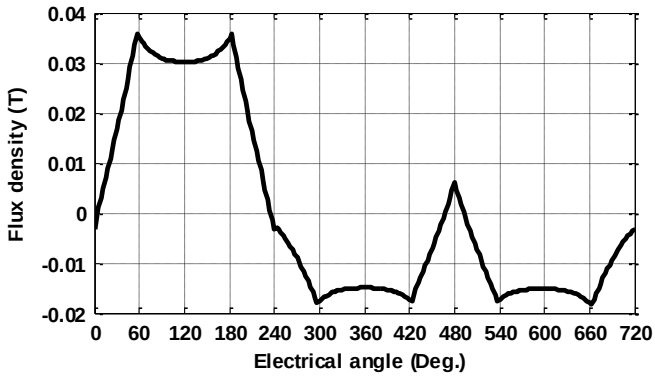

Fig. 9 *Axial component of armature reaction flux density: Ia = 8.48 A, Ib = Ic = -4.24 A*

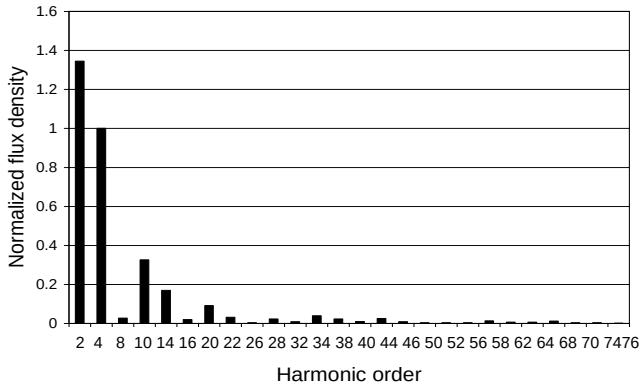

Fig. 10 *Normalized armature reaction harmonic flux density in AFPMSG*

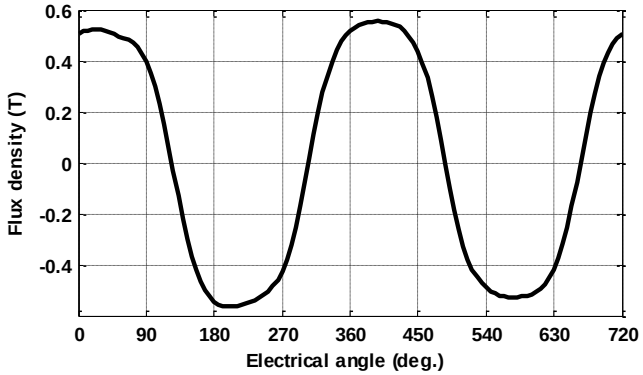

Fig. 11 *Axial component of resultant flux density: Ia = 8.48 A, Ib = Ic = -4.24 A*

Analytical computation of the synchronous reactance for an AFPMSG with coreless armature is difficult since there is no clear distinction between the armature reaction flux and leakage flux. This difficulty may be overcome by using the time-stepping FEA. With the magnetization on the permanent magnets removed and the rotor running at rated speed, balanced rated sinusoidal current I at rated frequency is injected into each phase of the armature winding. The resultant fundamental flux per pole Φ, and hence the induced e.m.f. E_a, is then determined. The armature reactance is then given by

$$X_s = \frac{E_a}{I} + X_e \tag{7}$$

where X_e is the end winding leakage reactance, computed using the method reported by Gieras and Wang [32].

By using the above method, the end winding leakage reactance and synchronous reactance of the prototype AFPMSG were found to be 0.02 Ω and 0.99 Ω, respectively. The synchronous impedance Z_s of the AFPMSG is thus equal to (0.93 + j0.99) Ω.

4.3 Voltage and current waveforms

The performance of the generator when supplying an isolated, three-phase three-wire resistive load was computed with the time-stepping, coupled field-circuit, 2-D FEA. Fig. 12 presents the computed waveforms of the phase voltage and line voltage with the machine on no load. The peak values of the line voltage and phase voltage are 69.3 V and 36.1 V, respectively. Because of the large third harmonic component in the air gap flux density B_z, there is a flat-topped phase voltage waveform. However, due to a three-phase, three-wire, star-connected load, the line voltages are practically sinusoidal. A harmonic analysis on the phase voltage waveform shows that the 3rd and 5th harmonic voltages are 11.6% and 1.1% of the fundamental.

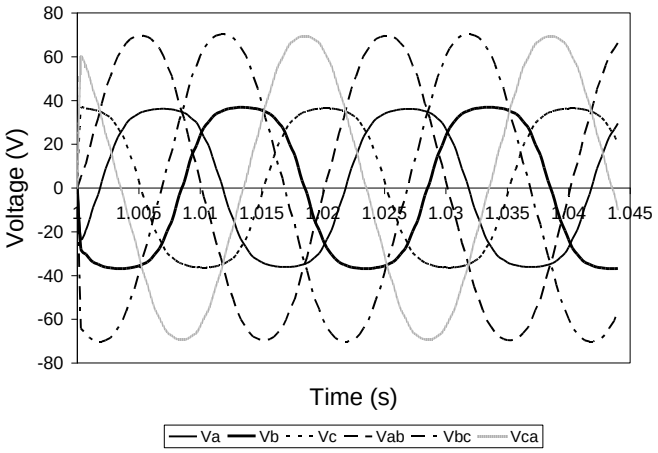

Fig. 12 *Line voltage and phase voltages of AFPMSG on no load at rated speed with a 2-D FEA study*

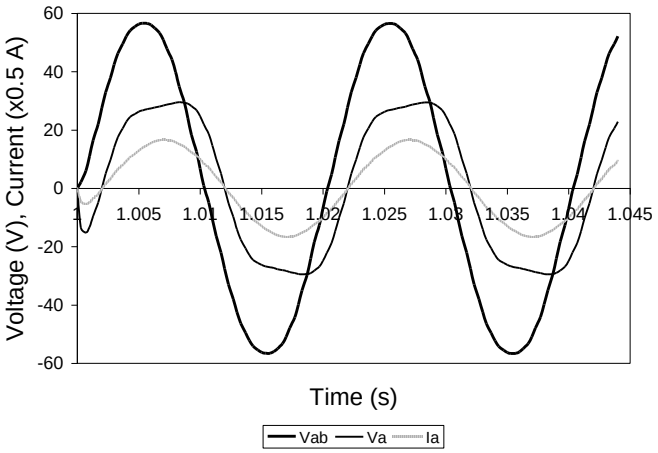

Fig. 13 *Simulated line voltage, phase voltage and line current waveforms at rated load current and rated speed*

Fig. 13 presents the simulated waveforms of line voltage, phase voltage and line current when the generator is driven at rated speed and is delivering rated current to a balanced three-wire pure resistive load. The peak values of line and phase voltage as well as line current are 56.6 V, 29.5 V and 8.33 A, respectively. With comparison of Fig. 12, the phase voltage waveform is now much more distorted and becomes asymmetrical. However, the waveforms of both the line voltage and the line current still remain approximately sinusoidal. The 3rd and 5th harmonic voltages are 14.5% and 1.0% of the fundamental, respectively.

4.4 Computation of torque

To obtain correct force information of the armature conductors, the air bands are meshed as rectangular elements with a uniform thickness of 0.17 mm. The force boundary is directly applied to the conductor region, and forces are computed during the FEA and stored in the air elements adjacent to the conductor region. During the post-processing stage, a macro is used to select and retrieve the force information stored in these air elements (computed using the virtual work method or Maxwell's stress method) and move them to the specified element table items. The total force is obtained by summing the element table items for each air element. Finally, the torque is obtained by multiplying the total force by the winding radius.

Fig. 14 shows the computed torque of the AFPMSG at rated load and rated speed. The torque computation results show that there is a

six-harmonic pulsating torque component superimposed on the average torque. The cause of this pulsating torque phenomenon may be explained as follows. Assume that the armature winding is feeding a balanced, passive resistive load. When the rotor is driven at normal speed n_s, balanced three-phase currents at fundamental frequency flow in the stator armature winding. Due to winding asymmetry, the armature reaction field contains considerable 5th and 7th harmonic components. The 5th space harmonic field rotates at speed 1/5 n_s in the opposite direction as the rotor, while the 7th harmonic field rotates at a speed 1/7 n_s in the same direction as the rotor. The 5th harmonic space field thus glides past the rotor field at a speed of $(1 + 1/5)n_s = (6/5)n_s$. Thus the resultant torque is not constant, but varies at a frequency of $f' = (6/5)n_s \times (5p) = 6n_sp = 6\ f_1$, where $f_1 = n_s.p$ = fundamental frequency.

The 7th harmonic component of the armature reaction m.m.f, however, glides past the rotor field at a speed $(1 – 1/7)n_s = 6/7\ n_s$. The frequency of pulsating torque is thus $(6/7)n_s \times (7p) = 6\ n_s.p = 6\ f_1$.

Now consider the fundamental component of the armature m.m.f which rotates at speed n_s in the forward direction. The armature reaction is in synchronism with the rotor field, hence a constant torque is produced.

It is seen that the 5th and 7th harmonic components of armature reaction m.m.f interact with the fundamental rotor field to produce a sixth harmonic torque pulsation in the prototype AFPMSG. From Fig. 14, the torque pulsation is only 2.8% of the average rated torque (13 N·m) as both the 5th and 7th harmonic m.m.f.s are quite small.

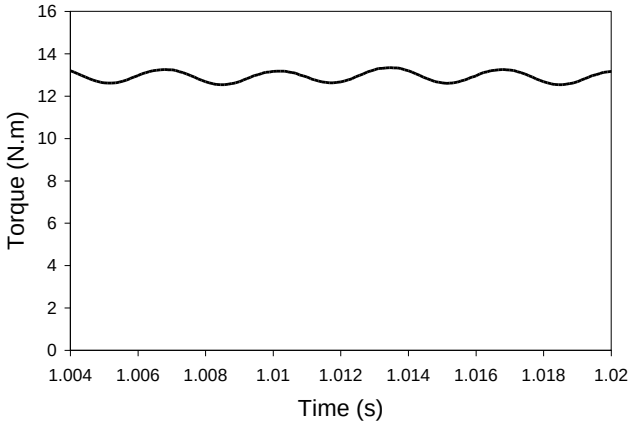

Fig. 14 *Computed steady-state electromagnetic torque of AFPMSG when delivering rated current at rated speed*

5 Experimental Results and Discussions

Similar experiments were carried out as described in [29], but with different operating conditions using the time-stepping 2-D FEA. The AFPMSG is assumed to operate at rated speed (375 r/min) with pure resistive loads supplied. Load tests were subsequently carried out with experimental setup as shown in Fig. 15. Fig. 16 presents the load characteristics obtained at rated speed. For comparison, the computed characteristic obtained from the synchronous impedance method is plotted as well. Due to the small leakage inductance and relatively weak effect of armature reaction, the variation of the terminal voltage depends primarily on the armature resistance drop. Accordingly, the external characteristics are practically linear from no load to full load. At rated current (6.0 A), the line voltage decreases to 40 V, which represents a 20% drop compared with the no-load voltage. The results show that the FEA gives a better prediction of the load characteristic of the AFPMSG than the synchronous impedance method.

Fig. 17 shows the computed and experimental variations of output power and efficiency with load current at rated speed. Maximum efficiency of the AFPMSG occurs at a relatively light load due to the small constant losses (7.85 W for this prototype machine). At rated current, the computed output of the generator is 396 W at 38 V with an efficiency of 78.3%. The computed and experimental results agree quite well despite some inaccuracies in output torque measurements.

Fig. 18 shows the experimental phase voltage waveform of the AFPMSG on no load. It is as predicted from FEA (Fig. 12). The peak value of the experimental no-load phase voltage is 36.3 V, which is very close to that computed by FEA.

Fig. 19 shows the experimental waveforms of phase voltage and line current at rated load current. Fig. 20 shows the experimental waveforms of line voltage and line current when driven at rated load current. The waveforms further confirm the results computed from FEA (Fig. 13). For instance, the measured peak values of line voltage and line current are 54.4 V and 7.8 A as compared with the computed values of 56.6 V and 8.3 A, respectively.

AFPMSG are available in a wide range of configurations. The common design process of the generator depends on numerical field analysis, due to the lack of analytical and/or empirical formulas especially for field distribution. When designing the generator with the compactness and high power density, a three-dimensional finite element analysis (3-D FEA) or 3-dimensional analytical or semi-analytical expressions is generally required [29, 33-35]. Even if numerical means are very useful to evaluate the mechanical properties of structures using ring permanent magnets, as pointed out in [33] that analytical or semi-analytical expressions are much more helpful because they have a low computational cost. Two-dimensional semi-analytical expressions have been proposed for the magnetic field created by ring permanent magnets. Although, the 2-D analytical approach allows an easy optimization of the ring dimensions but this approach is not very precise. A three-dimensional method was proposed for optimizing parameters such as inner radius of inner ring, outer radius of outer ring, axial displacement and air-gaps to create a very good axial passive magnetic bearing. The determination of the optimal width of the inner ring permanent magnet and influence of the air gap dimension on the axial force and the axial stiffness must be studied in detail. 3-D finite element analysis [29, 34, 35] will also be included to make comparison in terms of the configuration design accuracy and use of computation time. Also the generator is often linked to a rectifier to provide a DC power supply. When such a system is used for variable speed applications, it is desirable to extend the operation speed range. Since the induced voltage of the generator increases with the speed, the use of flux weakening control restricts the AFPMSG output voltage at high speed. This consequently increases the maximum operation speed and should be fully investigated to determine its impact on any change in properties of the generator [36-38]. These investigations will form part of the future work.

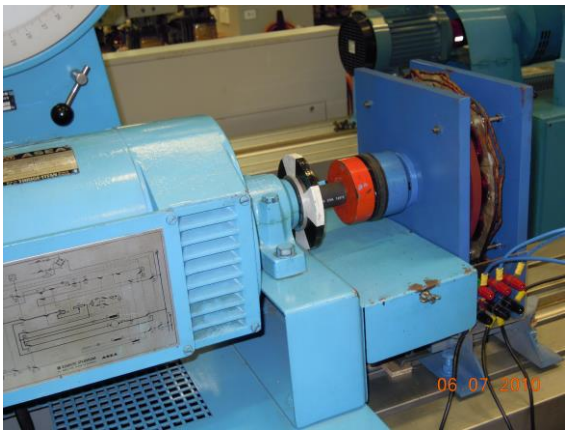

Fig. 15 *Experimental setup for load test on the AFPMSG*

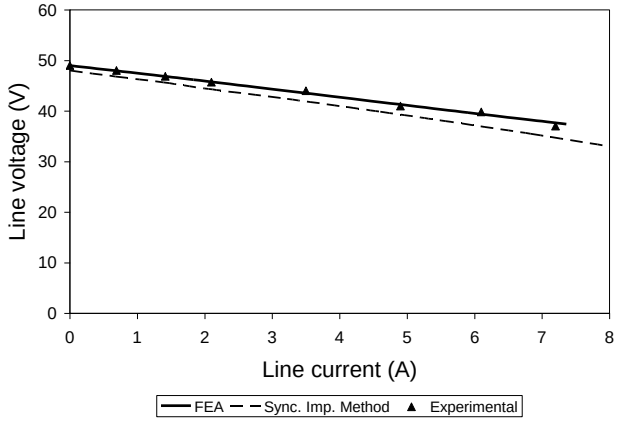

Fig. 16 *Load characteristics of AFPMSG at rated speed*

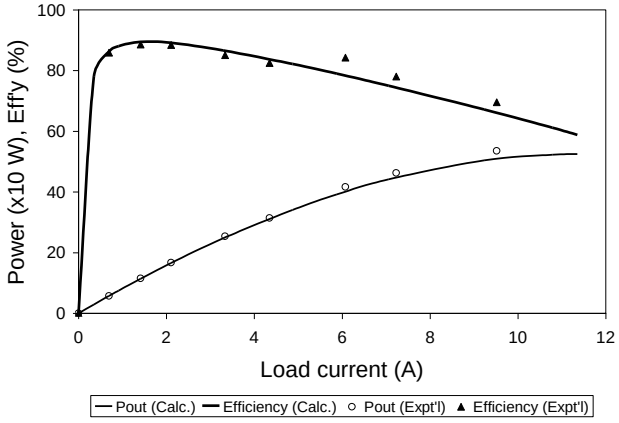

Fig. 17 *Output power and efficiency of AFPMSG at rated speed*

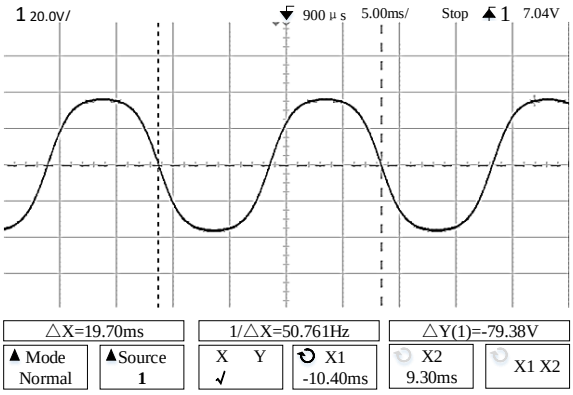

Fig. 18 *Experimental no-load waveform of phase voltage (Voltage scale: 20 V/div, time scale: 5 ms/div)*

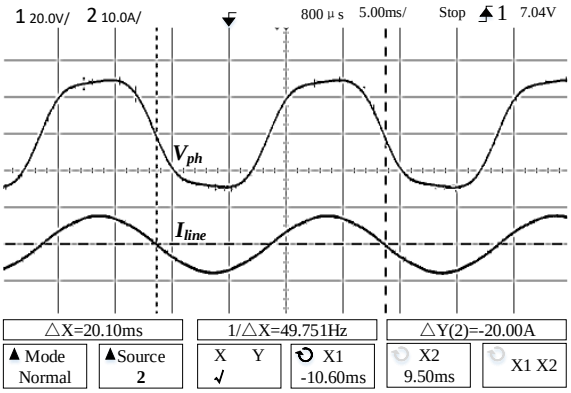

Fig. 19 *Experimental waveforms of phase voltage and line current at rated load (Voltage scale: 20 V/div, current scale: 10 A/div, time scale: 5 ms/div)*

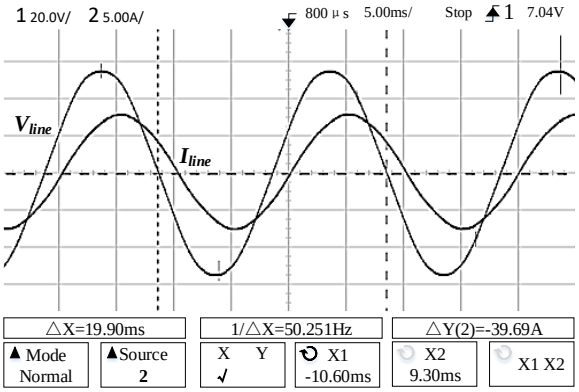

Fig. 20 *Experimental* waveforms of *line voltage and line current (Voltage scale: 20 V/div, current scale: 5 A/div, time scale: 5 ms/div)*

6 Conclusion

This paper presents the magnetic field distribution and performance of an Axial-Flux Permanent-Magnet Synchronous Generator with double-sided rotor and coreless armature based on a two-dimensional finite element analysis. The analysis has taken into consideration the asymmetry of the armature winding with respect to the rotor field, due to the non-integral ratio of coil number to pole number of the concentrated-coil winding. Armature reaction and its effect on torque ripples are also studied. The simulated results are verified through practical experiments on the prototype generator.

7 Acknowledgment

Financial supports from the Guangdong Province Science and Technology Planning Project under the Grant nos. 2016B090912006; the Guangdong University of Technology, Guangzhou, China under Grant from the Financial and Education Department of Guangdong Province 2016[202]: Key Discipline Construction Programme; the Education Department of Guangdong Province: New and Integrated Energy System Theory and Technology Research Group, Project Number 2016KCXTD022 and National Natural Science Foundation of China under Grant Number 61572201 are acknowledged.

8 References

[1] Wang, D., Gao, X., Meng, K., *et al.*:'Utilisation of kinetic energy from wind turbine for grid connections: a review paper', IET Renew. Power Gener., 2018, 12, (6), pp. 615-624.

[2] Xu, G., Xu, L., Morrow, J.:'Power oscillation damping using wind turbines with energy storage systems', IET Renew. Power Gener., 2013, 7, (5), pp. 449-457.

[3] Huang, C.-M., Chen, S.-J, Yang, S.-P. *et al.*:'Capacity optimisation for an SAMS considering LCOE and reliability objectives', IET Renew. Power Gener., 2018, 12, (7), pp. 787-796.

[4] 'Annual market update 2015', http://www.gwec.net, accessed May 2018.

[5] 'Global Wind Report 2016- Annual market update', http://gwec.net/publications/global-wind-report-2/global-wind-report-2016/, accessed May 2018.

[6] 'Global wind energy outlook 2016', http://www.gwec.net, accessed May 2018.

[7] 'Wind Power in Denmark', https://en.wikipedia.org/wiki/Wind_power_in_Denmark, accessed May 2018.

[8] Muljadi, E.C., Butterfield, P., Wan, Y.-H.:'Axial-flux modular permanent-magnet generator with a toroidal winding for wind-turbine applications', IEEE Trans. Ind. Appl., 1999, 35, (4), pp. 831-836.

[9] Chalmers, B., Spooner, E.:'An axial-flux permanent-magnet generator for a gearless wind energy system', IEEE Trans. Energy Convers., 1999, 14, (2), pp. 251-257.

[10] Lombard, N., Kamper, M.:'Analysis and performance of an ironless stator axial flux PM machine', IEEE Trans. Energy Convers., 1999, 14, (4), pp. 1051-1056.

[11] Wanjiku, J., Khan, M., Barendse, P.S., Pillay, P.:'Influence of slot openings and tooth profile on cogging torque in axial-flux PM machines', IEEE Trans. Ind. Electron., 2015, 62, (12), pp. 7578-7589.

[12] Bumby, J., Martin, R.:'Axial-flux permanent-magnet air-cored generator for small-scale wind turbines', IEE Proc.-Electr. Power Appl., 2005, 152, (5), pp. 1065-1075.

[13] Polinder, H., Van der Pijl, F.F.A., De Vilder, G.-J., Tavner, P.J.:'Comparison of direct-drive and geared generator concepts for wind turbines', IEEE Trans. Energy Convers., 2006, 21, (3), pp. 725-733.

[14] Azzouzi, J., Barakat, G., Dakyo, B.:'Quasi-3-D analytical modeling of the magnetic field of an axial flux permanent-magnet synchronous machine', IEEE Trans. Energy Convers., 2005, 20, (4), pp. 746-752.

[15] Brisset, S., Vizireanu, D., Brochet, P.:'Design and optimization of a nine-phase axial-flux PM synchronous generator with concentrated winding for direct-drive wind turbine', IEEE Trans. Ind. Appl., 2008, 44, (3), pp. 707-715.

[16] Xia, B., Shen, J.-X., Luk, P.C.-K., Fei, W.:'Comparative study of air-cored axial-flux permanent-magnet machines with different stator winding configurations', IEEE Trans. Ind. Electron., 2015, 62, (2), pp. 846-856.

[17] Polikarpova, M., Ponomarev, P., Lindh, P., *et al.*:'Hybrid cooling method of axial-flux permanent-magnet machines for vehicle applications', IEEE Trans. Ind. Electron., 2015, 62, (12), pp. 7382-7390.

[18] Caricchi, F., Crescimbini, F., Honorati, O., Bianco, G.L., Santini, E.:'Performance of coreless-winding axial-flux permanent-magnet generator with power output at 400 Hz, 3000 r/min', IEEE Trans. Ind. Appl., 1998, 34, (6), pp. 1263-1269.

[19] Wang, R.-J., Kamper, M.J.:'Calculation of eddy current loss in axial field permanent-magnet machine with coreless stator', IEEE Trans. Energy Convers., 2004, 19, (3), pp. 532-538.

[20] Javadi, S., Mirsalim, M.:'Design and analysis of 42-V coreless axial-flux permanent-magnet generators for automotive applications', IEEE Trans. Magn., 2010, 46, (4), pp. 1015-1023.

[21] Fei, W., Luk, P.C.-K., Jinupun, K.:'Design and analysis of high-speed coreless axial flux permanent magnet generator with circular magnets and coils', IET Electr. Power Appl., 2010, 4, (9), pp. 739-747.

[22] Zhang, B., Seidler, T., Dierken, R., Doppelbauer, M.:'Development of a yokeless and segmented armature axial flux machine', IEEE Trans. Ind. Electron., 2016, 63, (4), pp. 2062-2071.

[23] Ni, R., Wang, G., Gui, X., Xu, D.:'Investigation of d-and q-axis inductances influenced by slot-pole combinations based on axial flux permanent-magnet machines', IEEE Trans. Ind. Electron., 2014, 61, (9), pp. 4539-4551.

[24] Vansompel, H., Sergeant, P., Dupré, L., Van den Bossche, A.:'Axial-flux PM machines with variable air gap', IEEE Trans. Ind. Electron., 2014, 61, (2), pp. 730-737.

[25] Bumby, J. R., Martin, R., Mueller, M., *et al.*:'Electromagnetic design of axial-flux permanent magnet machines', IEE Proc.-Electr. Power Appl., 2004, 151, (2), pp. 151-160.

[26] Kamper, M.J., Wang, R.-J., Rossouw, F.G.:'Analysis and performance of axial flux permanent-magnet machine with air-cored nonoverlapping concentrated stator windings', IEEE Trans. Ind. Appl., 2008, 44, (5), pp. 1495-1504.

[27] Chan, T.F., Lai, L.L., Xie, S.:'Field computation for an axial flux permanent-magnet synchronous generator', IEEE Trans. Energy Convers., 2009, 24, (1), pp. 1-11.

[28] Zou. T., Li, D., Qu R., Li, J., Jiang, D.:'Analysis of a dual-rotor, toroidal-winding, axial-flux vernier permanent magnet machine', IEEE Trans. Ind. Appl., 2017, 53, (3), pp. 1920-1930.

[29] Chan, T.F., Wang, W., Lai, L.L.:'Performance of an axial-flux permanent magnet synchronous generator from 3-D finite-element analysis', IEEE Trans. Energy Convers., 2010, 25, (3), pp. 669-676.

[30] Chan, T.F., Lai, L.L.:'An axial-flux permanent-magnet synchronous generator for a direct-coupled wind-turbine system', IEEE Trans. Energy Convers., 2007, 22, (1), pp. 86-94.

[31] Chan, T.F., Wang, W., Lai, L.L.:'Magnetic field in a transverse- and axial-flux permanent magnet synchronous generator from 3-D FEA', IEEE Trans. Magn., 2012, 48, (2), pp. 1055-1058.

[32] Gieras, J. F., Wang R.-J., Kamper, M.J.:'Axial flux permanent magnet brushless machines' (Springer, The Netherlands, 2004, 2nd edn. 2008).

[33] Ravaud, R., Lemarquand, G., Lemarquand, V.:'Force and stiffness of passive magnetic bearings using permanent magnets. Part 1: axial magnetization', IEEE Trans. Magn., 2009, 45, (7), pp. 2996-3002.

[34] Daghigh, A., Javadi, H., Torkaman, H.:'Design optimization of direct-coupled ironless axial flux permanent magnet synchronous wind generator with low cost and high annual energy yield', IEEE Trans. Magn., 2016, 52, (9).

[35] Ishikawa, T., Amada, S., Segawa, K., Kurita, N.:'Proposal of a radial- and axial-flux permanent-magnet synchronous generator', IEEE Trans. Magn., 2017, 53, (6).

[36] Milivojevic, N., Schofield, N., Stamenkovic, I., Gurkaynak, Y.:'Field weakening control of PM generator used for small wind turbine application', IET Conf. on Renewable Power Generation (RPG 2011), Edinburgh, UK, Sept. 2011, pp. 1-8.

[37] Bozhko, S., Rashed, M., Hill C.I., Yeoh, S.S., Yang, T.:'Flux-weakening control of electric starter-generator based on permanent-magnet machine', 2017, IEEE Trans. on Transportation Electrification, 3, (4), pp. 864-877.

[38] Miao,D.-M., Shen, J.-X.:'Simulation and analysis of a variable speed permanent magnet synchronous generator with flux weakening control', 2012 International Conf. on Renewable Energy Research and Applications (ICRERA), Nagasaki, Japan, Nov. 2012, pp. 1-6.

9 Appendix

Specifications of the prototype AFPMSG:

Output at nominal speed

400 W, 38 V, 6.0 A, 50 Hz at 375 rpm

Rotor field (each disk)

Number of poles	= 16
Outer radius	= 100 mm
Inner radius	= 58 mm
Thickness of magnets	= 5 mm
Pole arc at mean radius	= 160^0e
Remanent flux density	= 1.21T
Recoil permeability of magnets	= 1.05
Thickness of each rotor yoke	= 10 mm

Armature winding and air gap

Winding type	= 3 phase star, single layer, concentrated
Number of coils	= 12
Turns per coil	= 60
Armature resistance at 75^0C	= 0.93 Ω
Leakage inductance of end winding	= 1.78^{-5} H
Thickness of winding	= 10 mm

Physical air gap length	= 2 x 0.5 mm

Mass of active materials

Copper	= 3.82 kg
Iron	= 5.97 kg
Magnets	= 1.37 kg